Article

Dynamic Measurements with the Bicone Interfacial Shear Rheometer: Numerical Bench-Marking of Flow Field Based Data Processing

Pablo Sánchez-Puga [1,‡], Javier Tajuelo Rodríguez [1,2,3,†,‡], Juan Manuel Pastor [4,‡], and Miguel Ángel Rubio [1,‡]

1 Dpto. Física Fundamental, Fac. Ciencias, Universidad Nacional de Educación a Distancia (UNED), Senda del Rey 9, Madrid 28040; p.sanchez@fisfun.uned.es; mar@fisfun.uned.es
2 Dpto. Física Aplicada, Fac. Ciencias, Universidad de Granada, Avenida Fuente Nueva s/n, Granada 18071; j.tajuelo.rodriguez@gmail.com
3 Dpt. of Chemichal Engineering, Stanford University, USA
4 Grupo de Sistemas Complejos, ETSIAAB, Universidad Politécnica de Madrid, Av. Puerta de Hierro 4, Madrid 28040; juanmanuel.pastor@upm.es
* Correspondence: p.sanchez@fisfun.uned.es; Tel.: +34-91-398-7129
† Current address: Affiliation 3
‡ These authors contributed equally to this work.

Version October 8, 2018 submitted to Preprints

Abstract: Flow field based methods are becoming increasingly popular for the analysis of interfacial shear rheology data. Such methods take properly into account the subphase drag by solving the Navier-Stokes equations for the bulk phases flows, together with the Boussinesq-Scriven boundary condition at the fluid-fluid interface, and the probe equation of motion. Such methods have been successfully implemented at the double wall-ring (DWR), the magnetic rod (MR), and the bicone interfacial shear rheometers. However, a study of the errors introduced directly by the numerical processing is still lacking. Here we report on a study of the errors introduced exclusively by the numerical procedure corresponding to the bicone geometry at an air-water interface. In our study we directly input a preset the value of the complex interfacial viscosity and we numerically obtain the corresponding flow field and the complex amplitude ratio for the probe motion. Then we use the standard iterative procedure to obtain the calculated complex viscosity value. A detailed comparison of the set and calculated complex viscosity values is made upon changing different parameters such as real and imaginary parts of the complex interfacial viscosity and frequency. The observed discrepancies yield a detailed landscape of the numerically introduced errors.

Keywords: interfacial rheology; interfacial shear rheometer; bicone interfacial rheometer; flow field based data processing.

---

1. Introduction

Complex interfacial fluid systems have received much attention in recent years because of their interest from, both, a fundamental and applied point of view in living and industrial systems [1]. Systems such as the tear film, the lung's internal fluid film, cell membranes, foams, and emulsions constitute examples of complex interfacial fluid systems whose dynamical properties play a crucial role regarding their function or utility. Indeed, knowledge of the mechanical properties of such fluid interfacial systems is an essential factor in the development of medical therapies in lung [2] or eye diseases [3], or in the stability and performance of industrial products in the food [4], personal care [5,6], and oil recovery sectors [7].

The characterization of the rheology (mechanical properties) of complex interfacial fluid systems is a powerful tool to unravel the physico-chemical phenomena occurring in interfacial processes [1]. A full characterization of the mechanical properties of plane interfacial systems requires studying the

Peer-reviewed version available at Colloids Interfaces 2018, 2, 69; doi:10.3390/colloids2040069

mechanical response in two deformation modes[8], namely, shear mode, that keeps the area constant while allowing for shape changes, and dilatational mode, that keeps the shape unchanged while allowing for area changes. In this report we will restrict ourselves to the shear deformation mode.

A very convenient way to characterize the dynamical viscoelasticity properties of complex fluid interfaces is through the low amplitude oscillatory motion of a probe located at the interface [9], which allows to describe the interface rheology in terms of a complex interfacial dynamic modulus, $G_s^*(\omega) = G_s'(\omega) + iG_s''(\omega)$, where $G_s'(\omega)$ accounts for the elastic component of the response and is called the interfacial storage modulus, and $G_s''(\omega)$ represents the viscous component of the response and is called the interfacial loss modulus. Alternatively, a complex interfacial viscosity can be defined as $\eta_s^*(\omega) = \eta_s'(\omega) - i\eta_s''(\omega) = iG_s^*(\omega)/\omega$, whose components are related to the interfacial dynamic moduli by $\eta_s' = G_s''/\omega$ and $\eta_s'' = G_s'/\omega$.

Many experimental realizations of such oscillating probe techniques have been proposed and, as of today, three of them emerge as largely popular configurations for Interfacial Shear Rheometers (ISR hereafter). Two of them are built around conventional rotational rheometers by using purposely designed fixtures: a bicone bob [10] or a double wall-ring (DWR hereafter) [11]. The third configuration uses a magnetic rod probe whose oscillation is forced by either a suitably driven Helmholtz coil pair [12] or a mobile magnetic tweezers actuator [13].

In all configurations the complex interfacial dynamic moduli or viscosities are obtained through the relationship between the amplitudes of the driving torque (or force) and angular (or linear) displacement, and their phase difference. However, subtracting the effect of the subphase drag on the probe motion is, both, of paramount importance and highly non-trivial. An indication of the relative importance of the interface and subphase drags on the probe is given by the complex Boussinesq number, Bo^*. For instance, in the case of an air/water interface Bo^* is defined as [14]:

$$Bo^* = \frac{\eta_s^*}{L\eta}, \tag{1}$$

where η_s^* is the complex interfacial viscosity, η is the subphase bulk viscosity and L is a characteristic length scale that depends on the geometric configuration of the rheometer. The pioneering work in Ref. [15] opened the way to use computed flow fields in the interpretation of the interfacial rheology data. A further step forward was taken by introducing an iterative scheme to recover the value of the complex interfacial viscosity using the computationally obtained flow field and the experimental values of the torque and angle amplitudes and relative phase in the DWR interfacial rheometer [11]. Since then, several flow field based data processing schemes, adequate for the magnetic rod ISR [13,16,17] and the bicone ISR [18], have been proposed to take properly into account the subphase drag on the probe.

Such schemes share a common structure, starting from a "seed" value of the complex interfacial viscosity, namely:

1. Solve the Navier-Stokes equations for the subphase flow field with no slip boundary conditions at the container and probe walls, and the Boussinesq-Scriven boundary condition at the interface.
2. Use the obtained flow field to compute the subphase and interface drags on the probe.
3. Use the probe equations of motion to obtain a new prediction for the value of the complex interfacial viscosity.
4. Go back to step 1 till convergence is obtained for the value of the complex interfacial viscosity.

Such schemes have rendered excellent results in the DWR [11], the magnetic rod ISRs, both in the Helmholtz coil [16] and the magnetic tweezers [13] configurations, and the bicone ISR [18], yielding good values of the complex interfacial viscosity and providing a more realistic separation of the real and imaginary parts of the complex interfacial viscosity.

From a practical point of view, an essential characteristic of each of the above mentioned ISRs is their respective measuring range in a parameter space defined by η_s', η_s'', and ω. In this aspect, assessing the performance of the flow field based iterative process is of paramount importance, particularly in the case of the bicone ISR, due to the comparatively higher role played by the subphase because of the larger subphase contact with the probe lower surface, that renders comparatively lower values of Bo^* [19]. Limited studies [18,20] of the available measuring range and the errors introduced by the iterative process have been made in the case of the bicone ISR.

Here we report on a more complete numerical bench-marking of the flow field based data processing scheme when applied to the bicone ISR. This study has been made using used a software package that we have recently made publicly available [21]. The software package uses an iterative scheme defined directly upon Bo^*, and makes extensive use of the sparse matrix functions in MATLAB.

In that purpose, we have defined two numerical problems, a direct one -given η_s', η_s'', and ω, find the complex amplitude ratio, AR^*- and an inverse one -given AR^* and ω find η_s' and η_s'' through the iterative process-. The software has been slightly modified so that the the flow field obtained with the "seed" η_s' and η_s'' values is used to obtain the complex amplitude ratio which is the solution of the direct problem.

Using the output of the direct problem as input of the inverse one, we have made a detailed study of the consistency of the iterative data processing scheme in terms of the differences appearing between the complex viscosity input values of the direct problem and the corresponding output values of the inverse problem. Further imposing the requirement that the complex amplitude ratio must be different from the one corresponding to a clean water interface allows us to draw a complete map of the parameter space available to the bicone ISR when using the flow field based data processing scheme.

2. Results

In this section we show the results obtained through extensive numerical calculations aiming at evaluating the performance of the iterative data processing scheme when applied to a bicone interfacial rheometer working in oscillatory mode at an air/water interface.

A careful evaluation of the dependence on the mesh size of the spatial velocity gradients representation, the number of iterations needed for convergence, and the computational costs of the procedure was reported in Ref. [20], where preliminary explorations of the consistency of the iterative data processing scheme, by sweeping in the complex interfacial viscosity while keeping ω constant were also included.

Here we will focus, first, on checking the consistency of the iterative processing scheme upon changes of the oscillation frequency in the typical range explored in real experiments, and, second, on analyzing the measuring range achievable with a bicone ISR when using the proposed flow field based data analysis scheme. This last aspect will be illustrated through the analysis of the achievable measuring range of a bicone fixture in our Bohlin C-VOR rheometer.

2.1. Consistency of the iterative data analysis scheme

2.1.1. Consistency over frequency range

We have studied the consistency of the iterative data analysis scheme through the following general procedure: i) Preset the frequency, f, and the complex interfacial viscosity, $\eta^*_{s\,prog}$ and solve the direct problem that yields the complex amplitude ratio AR^*_{prog}, and ii) use the obtained value of the complex amplitude ratio as input of the inverse problem and obtain the calculated value of the complex interfacial viscosity, $\eta^*_{s\,calc}$.

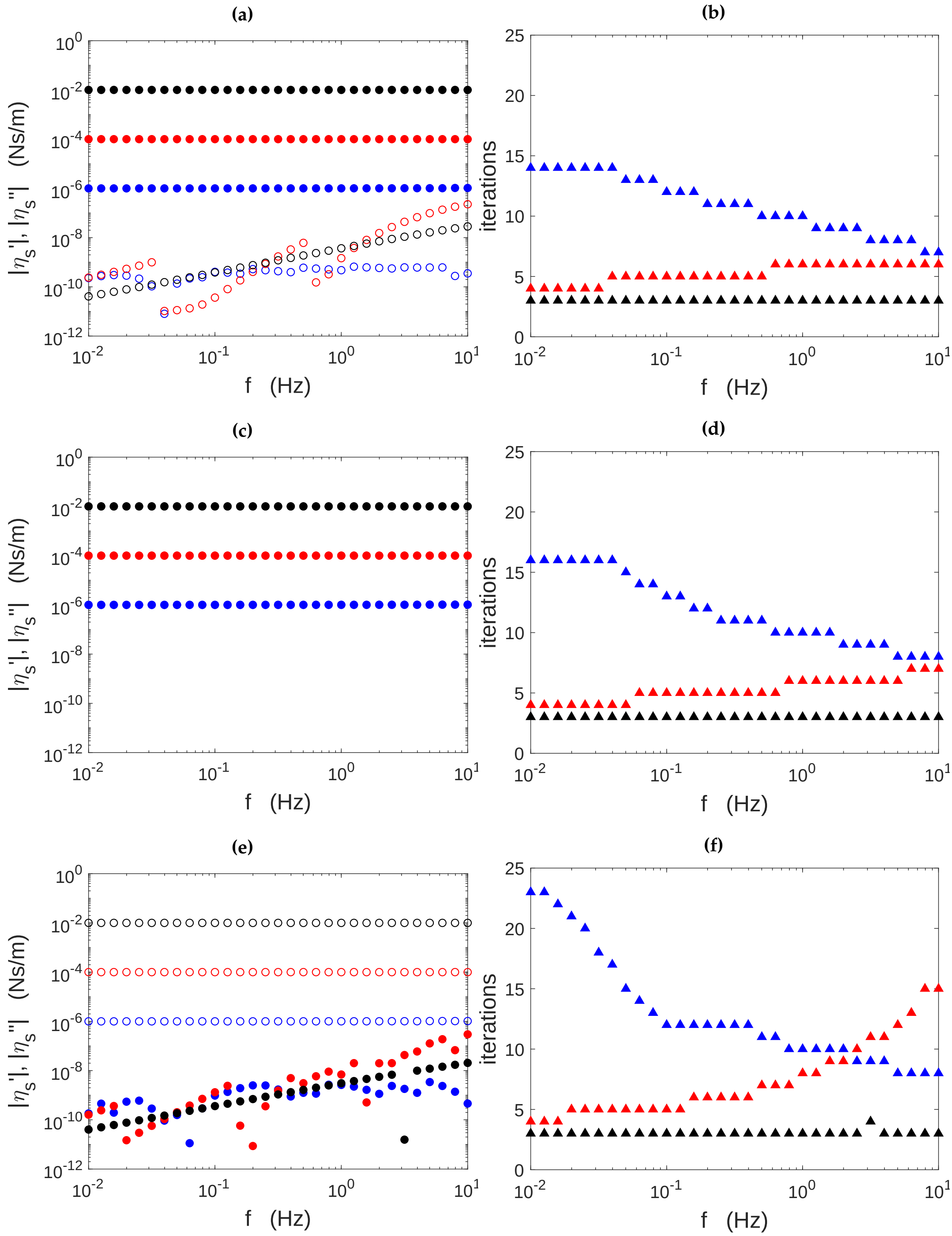

Figure 1. Values obtained for the complex interfacial viscosity (left column, graphs (**a**), (**c**), and (**e**)) and number of iterations needed for convergence (right column, graphs (**b**), (**d**), and (**f**)) as a function of frequency for purely viscous interfaces (top row, graphs (**a**) and (**b**)), viscoelastic interfaces (middle row, graphs (**c**) and (**d**)) and purely elastic interfaces (lower row, graphs (**e**) and (**f**)). In the graphs on the left column, filled and empty circles refer to the real and imaginary parts of the complex interfacial viscosity, respectively. Symbol's colours indicate the numerical value of η_s, namely, $\eta_s = 10^{-2}$ (black), $\eta_s = 10^{-4}$ (red), and $\eta_s = 10^{-6}$ (blue), in units of N s/m.

Preprints (www.preprints.org) | NOT PEER-REVIEWED | Posted: 8 October 2018 doi:10.20944/preprints201810.0139.v1

Peer-reviewed version available at Colloids Interfaces 2018, 2, 69; doi:10.3390/colloids2040069

In Fig. 1 we show the results of such a procedure for a frequency sweep in the range $10^{-2} \leq f \leq 10$ Hz. Representative values of the complex interfacial viscosity have been chosen, namely, a purely viscous interface ($\eta_s^* = \eta_s'$, i.e., $\eta_s'' = 0$), a viscoelastic interface ($\eta_s^* = \eta_s' - i\eta_s''$, where $\eta_s' = \eta_s''$), and a purely elastic interface ($\eta_s^* = -i\eta_s'$, i.e., $\eta' = 0$). Three typical numerical values of η_s have been used in the above described cases: $\eta_s = 10^{-6}, \eta_s = 10^{-4}, \eta_s = 10^{-2}$, in units of N s/m.

The graphs on the left column illustrate the results obtained for $\eta'_{s calc}$ and $\eta''_{s\ calc}$ as a function of frequency, while the right column holds the graphs of the number of iterations needed for convergence at each frequency. The graphs at the upper row (graphs (a) and (b)) pertain to the purely viscous interface, those at the middle row (graphs (c) and (d)) to the viscoelastic interface, and the lower row graphs ((e) and (f)) show the data corresponding to the purely elastic interface. In the left column graphs, filled and empty circles are used to represent the values of $\eta'_{s calc}$ and $\eta''_{s\ calc}$, respectively. Symbol's colours black, red, and blue correspond, respectively, to the high, middle, and low numerical values of η_s mentioned above.

The agreement between the obtained viscosity component values and the non null programmed values is remarkable (in the case of the viscoelastic interface solid and empty circles superpose as expected). However, unavoidable numerical errors and the finite convergence tolerance, given by the $tolMin$ parameter (Eq. 10), necessarily give rise to non null values of $\eta''_{s\ calc}$ for the purely viscous interface (graphs (a) and (b)) and $\eta'_{s calc}$ for the purely elastic interface (graphs (e) and (f)). Fortunately, these pathological non null values are in all of the cases here studied more than two orders of magnitude below their measurable counterparts ($\eta'_{s calc}$ for the purely viscous interface and $\eta''_{s\ calc}$ for the purely elastic interface).

The graphs on the right column show that in the studied frequency range, convergence in the inverse problem always occurs in less than 25 iterations. Particularly remarkable is the case with the higher complex viscosity modulus ($\eta_s = 10^{-2}$ N s/m, black symbols), where convergence occurs in three iterations for the whole frequency range. Interestingly, for intermediate values of the complex viscosity modulus (red symbols) increasing the frequency has a destabilizing effect (more iterations are required for convergence), while for very low complex viscosity modulus (blue symbols) the effect is just the opposite (less iterations are needed for convergence upon increasing the frequency).

The visual agreement between the obtained viscosity component values and the non null programmed values in the graphs on the left column of Fig. 1 can be better ascertained calculating the relative difference between the programmed and calculated values and representing it in a logarithmic vertical scale. Fig. 2 shows such graphs, where row arrangement and symbols' shapes and colours maintain the same codding as in Fig. 1. To be specific, the relative differences have been calculated as:

$$\delta_{\eta'} = 100 \times \left| \frac{\eta'_{s calc} - \eta'_{s prog}}{\eta'_{s prog}} \right| ; \quad \delta_{\eta''} = 100 \times \left| \frac{\eta''_{s\ calc} - \eta''_{s\ prog}}{\eta''_{s\ prog}} \right|$$

Several common features appear in the three graphs included in Fig. 2. First, the relative differences are overall increasing functions of frequency, although non monotonic in some cases. Second, the relative differences are higher the smaller the value of η_s' or η_s''. Nonetheless, such relative differences are of the order of a few percent in the worst case -lowest numerical value of η_s' or η_s'' and highest frequency value- and smaller in all of the other cases. In the case of the viscoelastic interface the relative differences are very similar in, both, the real and imaginary parts of the complex viscosity.

Preprints (www.preprints.org) | NOT PEER-REVIEWED | Posted: 8 October 2018 doi:10.20944/preprints201810.0139.v1

Peer-reviewed version available at *Colloids Interfaces* **2018**, *2*, 69; doi:10.3390/colloids2040069

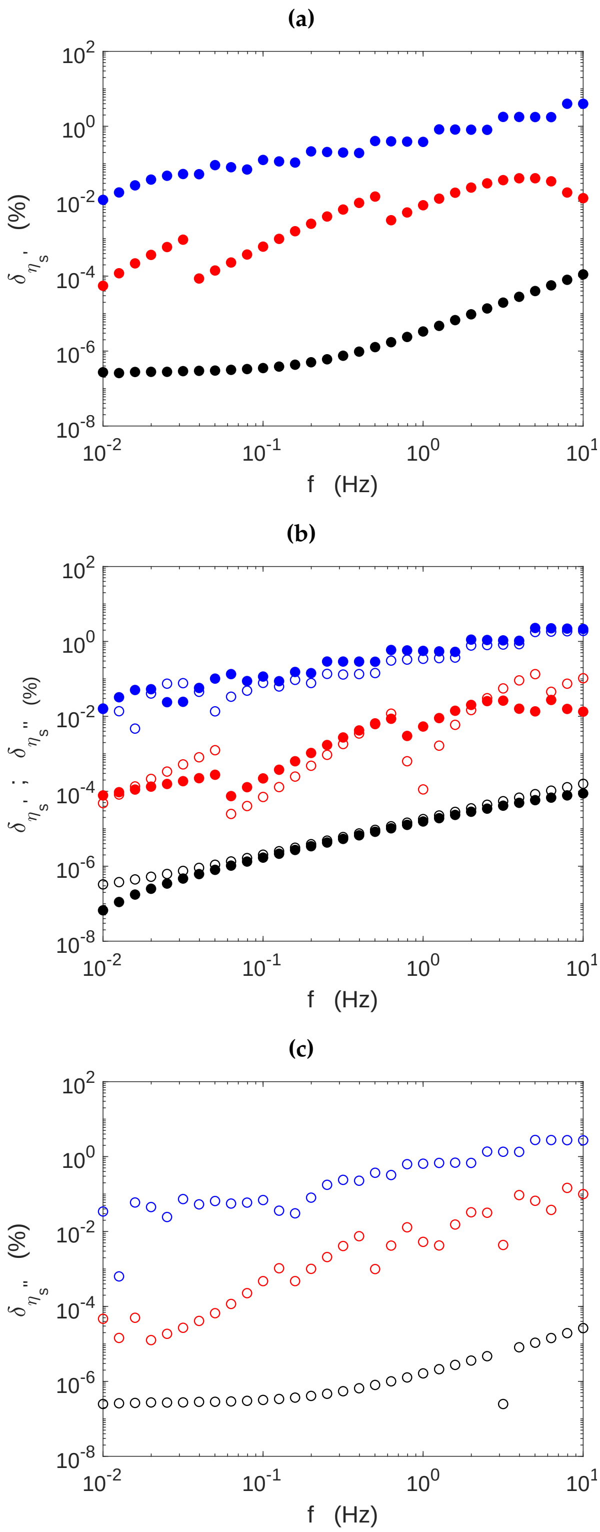

Figure 2. Relative errors obtained in the non null components of the complex interfacial viscosity as a function of frequency for: (**a**) purely viscous interfaces, (**b**) viscoelastic interfaces, and (**c**) purely elastic interfaces. Filled and empty circles refer to the real and imaginary parts of the complex interfacial viscosity, respectively. Symbols colours indicate the numerical value of η_s, namely, $\eta_s = 10^{-2}$ (black), $\eta_s = 10^{-4}$ (red), and $\eta_s = 10^{-6}$ (blue), in units of N s/m.

2.1.2. Consistency in the complex plane

A complementary view of the consistency problem can be drawn through the percentage modulus of the complex relative differences between $\eta^*_{s\,calc}$ and $\eta^*_{s\,prog}$, i.e.,

$$\delta_{mod} = 100 \times \left| \frac{\eta^*_{s\,prog} - \eta^*_{s\,calc}}{\eta^*_{s\,prog}} \right|$$

We have calculated the values of δ_{mod} at 60×60 logarithmically spaced points in the (η'_s, η''_s) plane, in the range $10^{-6} \leq \eta'_s, \eta''_s \leq 10^{-3}$ in units of N s/m, at three representative frequency values, namely, 0.1, 1, and 10 Hz. The values so obtained have been used to construct contour plots of δ_{mod} in the (η'_s, η''_s) plane, which are shown in Fig. 3. The contour lines correspond to the percentage values of δ_{mod} indicated in the caption.

Preprints (www.preprints.org) | NOT PEER-REVIEWED | Posted: 8 October 2018 doi:10.20944/preprints201810.0139.v1

Peer-reviewed version available at *Colloids Interfaces* **2018**, *2*, 69; doi:10.3390/colloids2040069

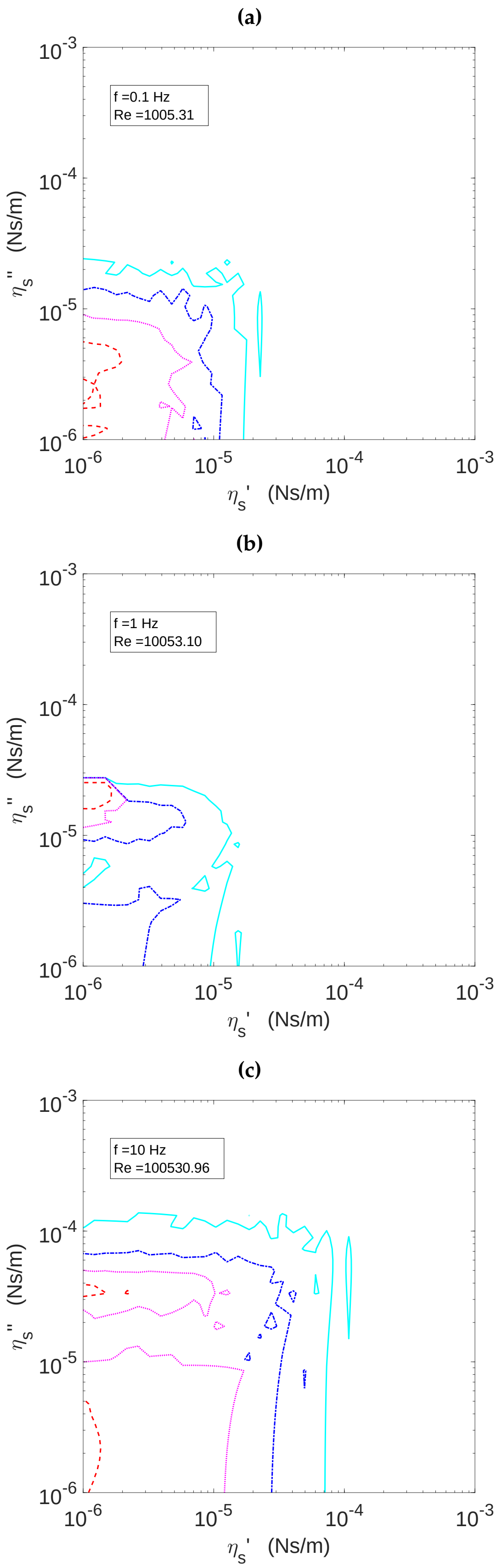

Figure 3. Contour plots of δ_{mod} in the (η_s', η_s'') plane at the frequency value indicated in the corresponding legend. The contour lines correspond to the following percentage values of δ_{mod}: (**a**) 0.01, 0.02, 0.04, 0.1. (**b**) 0.15, 0.3, 1, 30. (**c**) 0.2, 0.5, 1, 2. In the three graphs red dashed lines correspond to the highest δ_{mod} value and continuous light blue lines to the lowest δ_{mod} value.

The aspect of the contour lines is not smooth, with even the appearance of some islands. However, it might be possible that such islands are an artifact caused by the limited resolution of only 60×60 points in the (η_s', η_s'') plane, due to the high computational cost of these simulations.

However, some general observations can be done on Fig. 3. In the three cases here considered, the structure of the contour lines corresponding to the lower values of δ_{mod} (continuous light blue lines) is roughly square, while strong peaks (red dashed lines) appear close to the lower values of η_s' , i.e., in elasticity dominated interfaces.

Regarding the performance of the iterative data processing scheme it is important to look at the numerical values of δ_{mod} in each of the graphs having in mind that it represents the modulus of the relative difference between two values of the complex interfacial viscosity: the programmed value at the start of the direct problem and the calculated value at the end of the inverse problem.

In the (a) graph δ_{mod} takes very low values all of them being lower than 0.2%, while $\delta_{mod} \leq 0.1\%$ in the region such that $\eta_s' \geq 2 \times 10^{-6}$ and $\eta_s'' \geq 10^{-5}$ in units of N m/s. This means that the iterative process introduces very small errors ($\leq 0.1\%$) in the interfacial viscosity measurements within most of the (η_s', η_s'') range here considered provided they are made at low oscillation frequencies (0.1 Hz in the top graph).

In the (b) graph of Fig. 3 the values of δ_{mod} are much higher (up to 60% at the peak), while $\delta_{mod} \leq 0.15\%$ in the region such that $\eta_s' \geq 10^{-5}$ and $\eta_s'' \geq 3 \times 10^{-5}$. Hence, the (η_s', η_s'') range in which the iterative process introduces small errors decreases significantly at an oscillations frequency of 1 Hz.

This tendency is again clear in graph (c) of Fig. 3. Although the values of δ_{mod} are lower than in the previous case (about 2.5% at the peak), the low error region ($\delta_{mod} \leq 0.2\%$) shrinks again to values such that $\eta_s' \geq 10^{-4}$ and $\eta_s'' \geq 10^{-4}$ in units of N m/s.

2.2. Estimation of the achievable measuring range

To elucidate which is the achievable measuring range of a bicone ISR when using the proposed flow field based data analysis scheme two main aspects have to be considered. On the one hand the instrumental errors, i.e., the unavoidable dispersion in the torque and angular displacement data measured by the rheometer. On the other hand the rheometry point of view, i.e., the fact that for the measurements to be acceptable they must be distinguishable from those pertaining to a clean water interface. The interplay between these two aspects is illustrated here through the analysis of the achievable measuring range of a bicone fixture in a Bohlin C-VOR rheometer.

In oscillatory measurements, the output of the rheometer comprises the amplitudes of the torque and the angular displacement, and their relative phase, which are used to determine the experimental value of the amplitude ratio, AR^*_{exp}. Given a surfactant laden interface, the instrument can resolve its complex viscosity if the corresponding complex amplitude ratio can be distinguished from that pertaining to a clean water interface. In Ref. [18] this condition was formally expressed as two inequalities that, both, had to be fulfilled simultaneously.

$$\left| \left| AR^*_{exp} \right| - \left| AR^*_{clean} \right| \right| \geq \sigma \left(\left| AR^* clean \right| \right); \quad \left| \arg(AR^*_{exp}) - \arg(AR^*_{clean}) \right| \geq \sigma \left(\arg(AR^*_{clean}) \right). \tag{2}$$

In order to apply Eqs. 2 we have calculated both AR^*_{exp} and AR^*_{clean} for different η_s', η_s'' combinations (all the combinations of 120 values logarithmically spaced in each axis) and different frequencies. The corresponding values for the uncertainties $\sigma(|AR^*_{clean}|)$ and $\sigma(\arg(AR^*_{clean})$ were taken from experiments performed on clean water interfaces at the Bohlin C-VOR rheometer.

In Fig. 4(a) we show the lines satisfying the equality in Eq. 2, i.e., the lower resolvable limit, for frequencies in the range $0.1 \leq f \leq 100$ Hz. For a clearer view, the lines corresponding to three representative frequencies, namely, $f = 0.1$, 1, and 10 Hz, are shown in Fig. 4(b).

The structure of the non-measurable region has some common features at all frequencies, such as the spiky tongue that widens at lower values of the real and imaginary parts of the viscosity. The

Preprints (www.preprints.org) | NOT PEER-REVIEWED | Posted: 8 October 2018 doi:10.20944/preprints201810.0139.v1

Peer-reviewed version available at Colloids Interfaces 2018, 2, 69; doi:10.3390/colloids2040069

island like structures at the tips of the tongues are artifacts caused by the width of the tongue being comparable to the distance between sampled points in the (η_s', η_s'') plane. In fact such islands should actually correspond to points corresponding to a continuous tongue that is getting thinner and thinner. The tongues shift to cover larger values of η_s' and η_s'' as the frequency increases.

For viscosity dominated interfaces (very low η_s'') there is, at each frequency, a well defined threshold interfacial viscosity below which the interface is non-distinguishable from a clean water interface. Roughly speaking those thresholds are (in N s/m units) 2×10^{-6} for $f = 0.1$ Hz, 3×10^{-5} for $f = 1$ Hz, and 3×10^{-3} for $f = 10 Hz$. This behavior coincides with the results shown in Fig. 7.c of Ref. [18].

A different behavior is seen for viscoelastic interfaces. Let's consider viscoelastic interfaces with $\eta_s' = \eta_s''$ (points a the bisectrix of Fig. 4 either (a) or (b)). For low values of η_s, the points lay in the base of the tongue and, therefore, the interface is non-distinguishable from a clean water one. Increasing in $\eta_s' = \eta_s''$ the tongue crosses below the bisectrix and, therefore, the points at the bisectrix become distinguishable from a clean water interfaces. Upon further increasing $\eta_s' = \eta_s''$ the tongue turns up and crosses again the bisectrix in a region in which the tongue is already very narrow. Hence, a very narrow window appears in which the interface is again non-distinguishable from a clean water one. For $\eta_s' = \eta_s''$ values larger than those at the above mentioned window the interface is again distinguishable from clean water. This behavior coincides with the results shown in Fig. 7.b of Ref. [18].

For elasticity dominated interfaces ($\eta_s'' \gg \eta_s'$) one finds (see lines corresponding to $f = 0.1$ and 1 Hz) that at low values of η_s'' the interface is not distinguishable from a clean water one, and there is, at each frequency, a well defined threshold interfacial elastic component (η_s'') below which the interface is non-distinguishable from a clean water interface. Above the threshold value the interfacial viscoelasticity can be measured. This scenario coincides with the results shown in Figs. 4c and 4e of the Supporting information of Ref. [18] except that in those figures narrow tongues in which the interface is again non-distinguishable from a clean water one. This means that the sampling of the (η_s', η_s'') plane in Fig. 4 is not enough to fully represent the narrow parts of the tongues.

All of the above mentioned features come from the non-fulfillment of the condition on the moduli. At large frequencies, however, the non-fulfillment of the condition on the arguments in Eq. 2 causes an additional enlargement of the non-distinguishable region in elasticity dominated interfaces. For instance, the line corresponding to $f = 10$ Hz in Fig. 4(b) shows a bump at high values of η_s'' and comparatively lower values of η_s'. Actually, in our numerical simulations that bump appears at all frequency values above 2.5 Hz, and shifts upwards and rightwards upon increasing the frequency (see Fig. 4(a)). Indeed, as from our simulations, it cannot be discarded that for lower frequencies similar bumps appears too although at values $\eta_s' \leq 10^{-6}$ N s/m.

Preprints (www.preprints.org) | NOT PEER-REVIEWED | Posted: 8 October 2018 doi:10.20944/preprints201810.0139.v1

Peer-reviewed version available at *Colloids Interfaces* **2018**, *2*, 69; doi:10.3390/colloids2040069

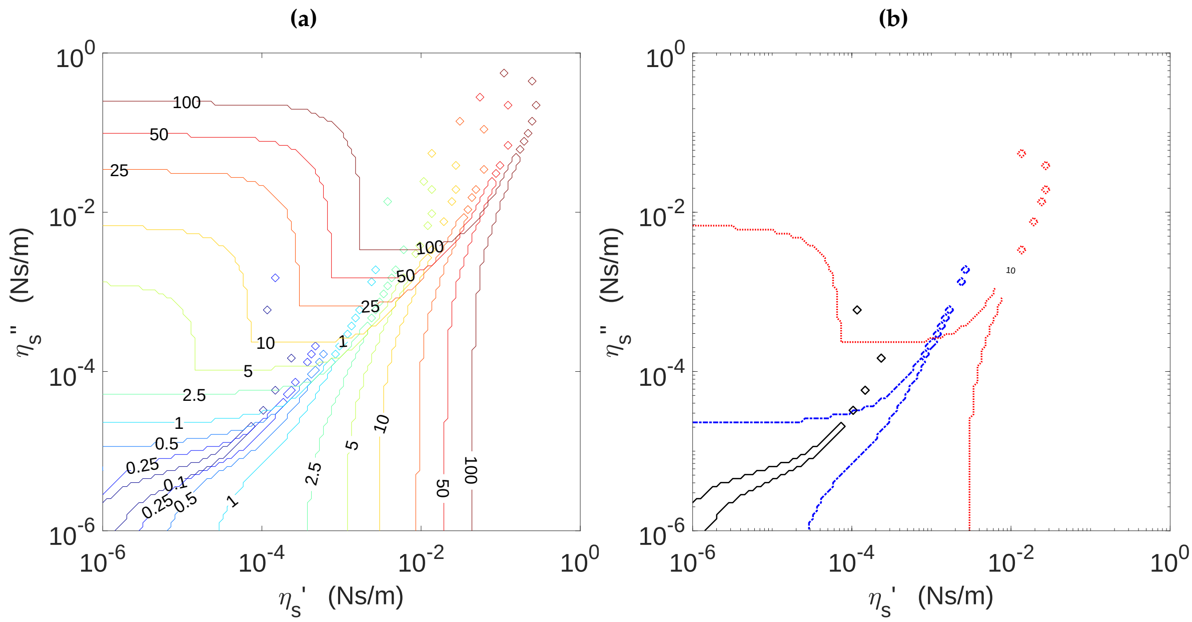

Figure 4. Boundaries separating the regions of the (η_s', η_s'') plane where the interface can be distinguished from a clean air-water interface, under fulfillment of both conditions in Eq. 2. (a) Lines at frequencies indicated by the line labels in the frequency range $0.1 \leq f \leq 100$ Hz. (b) Lines at representative frequencies: $f = 0.1$ Hz (black continuous line), $f = 1$ Hz (blue dash-dot line), and $f = 10$ Hz (red dotted line).

The distinguishability criterion based on simultaneous fulfillment of the two inequalities in Eq. 2 is, however, somewhat too strict. In fact, when any of the two inequalities is fulfilled the interface is already distinguishable from the clean water interface. If we use this relaxed criterion with the output of our simulations the picture so obtained is shown in Fig. 5, where both the resonance tongues, due to the condition on the moduli, and the bumps at the elasticity dominated region, due to the condition on the arguments, have disappeared.

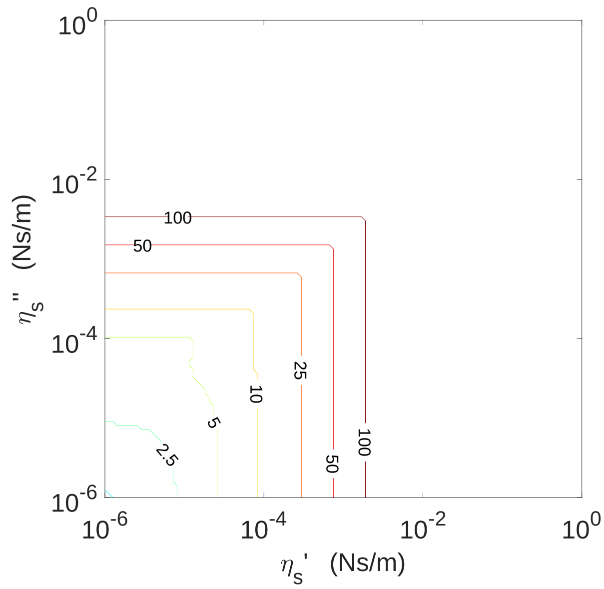

Figure 5. Boundaries separating the regions of the (η_s', η_s'') plane where the interface can be distinguished from a clean air-water interface, under fulfillment of either one of the conditions in Eq. 2. Lines at frequencies indicated by the line labels in the frequency range $0.1 \leq f \leq 100$ Hz.

Preprints (www.preprints.org) | NOT PEER-REVIEWED | Posted: 8 October 2018 doi:10.20944/preprints201810.0139.v1

Peer-reviewed version available at Colloids Interfaces 2018, 2, 69; doi:10.3390/colloids2040069

2.3. Global relative errors

In the previous subsections we have illustrated separately the errors introduced by the iterative process and the regions where interface can be distinguished from a clean water one. However, in actual experiments these two effects are coupled, because what one has as the result of an experiment is the values of the modulus and argument of the complex amplitude ratio, $\left|AR^*_{exp}\right|$ and $\delta_{exp} = \arg(AR^*_{exp})$, each one of then affected by its own experimental uncertainty, $\sigma\left(\left|AR^*_{exp}\right|\right)$ and $\sigma\left(\arg(AR^*_{exp})\right)$. So, the problem here is how the small area around the experimental values defined by the rectangle defined by the points $\left(\left|AR^*_{exp}\right| \pm \sigma\left(\left|AR^*_{exp}\right|\right), \delta_{exp} \pm \sigma\left(\arg(AR^*_{exp})\right)\right)$ transforms under the application of the iterative procedure.

In order to estimate that transformation, we program 60×60 $\eta'_{s\,prog}$ and $\eta''_{s\;prog}$ values in a logarithmic mesh in the $\left(\eta'_{s\,prog}, \eta''_{s\;prog}\right)$, and use them as input values for the direct problem, having as output the values of $\left|AR^*_{prog}\right|$ and δ_{prog}. For each of those data we use as uncertainty the experimental uncertainty measured for a clean water interface at the corresponding frequency, and define an enclosing rectangle with the points $\left(\left|AR^*_{prog}\right| \pm \sigma\left(\left|AR^*_{clean}\right|\right), \delta_{prog} \pm \sigma\left(\arg(AR^*_{clean})\right)\right)$. Next we use the corners of such a rectangle plus the middle points of the four rectangle faces as input of the inverse problem. Then, for each point in the plane $\left(\left|AR^*_{prog}\right|, \delta_{prog}\right)$ we now have eight images in the plane $(\eta'_{s\,iter}, \eta''_{s\;iter})$, that we label $\eta^{*i}_{s\;rect}$; $\;i = 1, ..., 8$, corresponding to the pertaining eight points that define the corresponding rectangle given by experimental uncertainties. Now, we define as a global error indicator, $\epsilon(\eta^*_{s\;prog})$, the maximal percentage relative difference between the programmed value of the complex interfacial viscosity, $\eta^*_{s\;prog}$, and the eight points $\eta^{*i}_{s\;rect}$, i.e.,

$$\epsilon(\eta^*_{s\;prog}) = 100 \times max\left\{\left|\frac{\eta^*_{s\;prog} - \eta^{*\;i}_{s\;rect}}{\eta^*_{s\;prog}}\right|\right\}, \tag{3}$$

The results of the application of such a procedure are shown en Fig. 6, for three representative frequencies, namely, $f = 0.1$ Hz, $f = 1$ Hz, and $f = 10$ Hz. In all of the three graphs, the contour lines, from right to left and top to bottom, correspond to the values $\epsilon(\eta^*_{s\;prog}) = 1, 5, 10, 20$ %.

Loosely speaking, if we take the 5% line as an acceptable error, the bicone fixture mounted in a Bohlin C-VOR rheometer with the flow field data processing scheme described in Ref. [18] can be expected to accurately measure complex interfacial viscosities (in Ns/m units) down to 2×10^{-5}, for $f = 0.1$ Hz, 3×10^{-4}, for $f = 1$ Hz, and 4×10^{-3}, for $f = 10$ Hz.

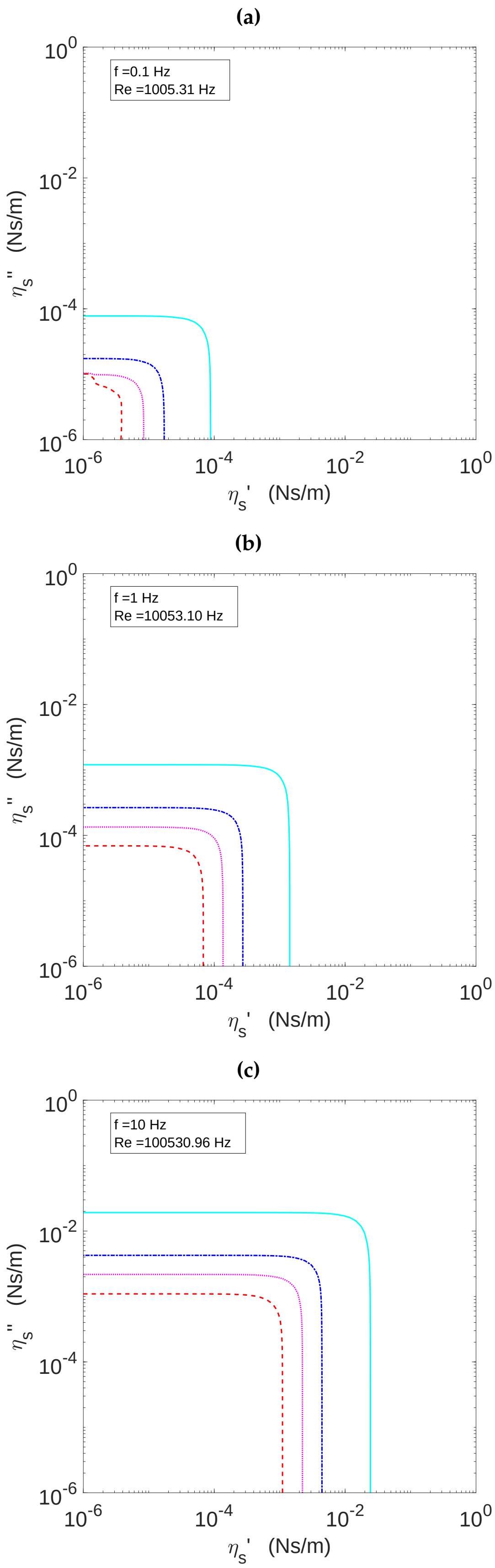

Figure 6. Contour plots of $\epsilon(\eta^*_{s\,prog})$ in the (η'_s, η''_s) plane at the frequency value indicated in the corresponding legend. The contour lines correspond to the following percentage values of $\epsilon(\eta^*_{s\,prog})$, values are 1, 5, 10, 20. In the three graphs red dashed lines correspond to the highest δ_{mod} value and continuous light blue lines to the lowest δ_{mod} value.

Peer-reviewed version available at Colloids Interfaces 2018, 2, 69; doi:10.3390/colloids2040069

3. Discussion

Apart from the comments already made while describing the results, several general questions deserve further discussion. First of all, why the solutions to the direct and the inverse problems may differ? In our opinion, the answer is that the direct and the inverse problems do not correspond to the same type of experiment. On the one hand, in the direct problem, the angular displacement of the probe is prescribed, which means the strain is prescribed and the probe equation of motion is used merely to obtain the corresponding complex amplitude ratio, i.e., the torque, which is directly related to the shear stress. In this sense the direct problem appears to be a strain controlled experiment.

On the other hand, in the inverse problem the complex amplitude ratio is prescribed and the iterative process yields the value of the complex interfacial viscosity and the complex velocity amplitude function that are compatible with the prescribed complex amplitude ratio. At each step of the iterative process, rotor inertia is taken into account, and, more importantly, changes in the complex velocity amplitude involve changes in the subphase and interface drag terms in Eq. 9. Therefore, the inverse problem appears to correspond closely to a stress controlled experiment. Hence, it is not so surprising that the solutions of the direct and inverse problems might differ somewhat.

Another aspect that deserves a comment is the remarkable frequency dependence of the peak values of δ_{mod} in Fig. 3, and which might be its origin. At low frequency values, fluid and rotor inertia do not play any role, and the velocity profile at the subphase and interface is linear. Hence, both the direct and the inverse problems have to give solutions very close to the linear velocity profile solution [18] and, therefore, the relative difference between their results must be small. At large frequency values, rotor inertia (the $I\omega^2$ term in Eqs. 8 and 9) dominates the dynamics, and the subphase and the interface do not play a leading role. Hence, the solutions of the direct and inverse problems must be again very similar, so that the values of the relative difference must be small here too. On the contrary, at intermediate frequency values, fluid inertia plays an essential role, the velocity profiles being strongly nonlinear and, more importantly, the inverse problem allows for variations in the velocity profile $g^*(\bar{r}, \bar{z})$ as iterations proceed, which may strongly affect the converged value of Bo^* and, hence, the value of $\eta^*_{s\,calc}$.

When resonance phenomena [18,20] appear large amplitudes, nonlinear behavior, and instabilities may occur. It is important to realize that the ansatz (Eq. 4) and the hydrodynamic model described in Section 4 allow us to obtain periodic fulfilling the ansatz. However, it is not guaranteed that such solutions are the only ones possible, neither that they are stable. Fully dynamical simulations of the probe equation of motion coupled to the hydrodynamic model should shed light on other possibly existing solutions and their stability.

4. Materials and Methods

4.1. Hydrodynamic model and data analysis scheme

The hydrodynamic model and data analysis scheme have been fully described elsewhere [20]. We reproduce it here just for the sake of completeness.

The interface is considered flat and horizontal, and the flow, both at the subphase and the interfaces is considered horizontal and axially symmetric. The angular oscillation of the bicone is considered periodic, with frequency ω. Hence, the bicone angular oscillation and the velocity at the bicone rim can be written as:

$$\theta(t) = \theta_0 e^{i\omega t}; \qquad v_\theta(R_b, h, t) = i\, R_b \omega \theta_0 e^{i\omega t}.$$

Under such approximations the spatial dependence of the fluid velocity field can be represented by a complex amplitude function $g^*(r,z)$ so that

$$v_\theta(r, z, t) = i\, R_b \omega g^*(r, z) \theta_0 e^{i\omega t}, \tag{4}$$

Preprints (www.preprints.org) | NOT PEER-REVIEWED | Posted: 8 October 2018 doi:10.20944/preprints201810.0139.v1

Peer-reviewed version available at Colloids Interfaces 2018, 2, 69; doi:10.3390/colloids2040069

where the spatial variables have been made non-dimensional taking R_b as characteristic length scale. The complex amplitude function must obey Eq. 5, derived from the Navier-Stokes equations, which in non-dimensional form read

$$i\,Re^*\,g^*(\bar{r},\bar{z}) = \frac{\partial^2 g^*(\bar{r},\bar{z})}{\partial \bar{r}^2} + \frac{\partial^2 g^*(\bar{r},\bar{z})}{\partial \bar{z}^2} + \frac{1}{\bar{r}}\frac{\partial g^*(\bar{r},\bar{z})}{\partial \bar{r}} - \frac{g^*(\bar{r},\bar{z})}{\bar{r}^2}, \tag{5}$$

where Re^* is the Reynolds number, $Re^* = \rho\omega R_c^2/\eta^*$ (possibly complex if the bulk subphase viscosity is complex). The boundary conditions are no-slip at the cup and bicone bob walls (Eq. 6) and the Boussinesq-Scriven boundary condition (tangential stress balance) at the interface (Eq.7) are

$$\begin{aligned} &g^*(\bar{r},0) = g^*(1,\bar{z}) = 0,\\ &g^*(0,\bar{z}) = 0,\\ &g^*(\bar{r} \le \bar{R}_b, \bar{h}) = \frac{\bar{r}}{\bar{R}_b}, \end{aligned} \tag{6}$$

$$\frac{\partial g^*}{\partial \bar{z}} = Bo^*\frac{\partial}{\partial \bar{r}}\left(\frac{1}{\bar{r}}\frac{\partial}{\partial \bar{r}}(\bar{r}\,g^*)\right), \text{ at } \bar{R}_b < \bar{r} < 1,\ \bar{z} = \bar{h}, \tag{7}$$

where $Bo^* = \eta_s^*/R_c\eta^*$.

The torque balance equation for the ISR rotor yields Eq. 8, that relates the complex amplitude ratio to, both, the Boussinesq number and, implicitly, the velocity amplitude function $g^*(\bar{r},\bar{z})$:

$$AR^* = i\omega 2\pi R_b\eta^*\left[\int_0^{R_b} r^2\left(\frac{\partial g^*}{\partial z}\right)\bigg|_{z=h} dr - R_b R_c Bo^*\left(R_b\left(\frac{\partial g^*}{\partial r}\right)\bigg|_{r=R_b,z=h} - 1\right)\right] - I\omega^2. \tag{8}$$

Solving for the Boussinesq number allows one to set up a simple iterative procedure, namely,

$$Bo^{*\{i+1\}} = \frac{-AR^*_{exp} - I\omega^2 + i\omega 2\pi R_b\eta^*\int_0^{R_b} r^2\left(\frac{\partial g^{*\{i\}}}{\partial z}\right)\Big|_{z=h} dr}{i\omega 2\pi\eta^* R_b^2 R_c\left(R_b\left(\frac{\partial g^{*\{i\}}}{\partial r}\right)\Big|_{r=R_b,z=h} - 1\right)}, \tag{9}$$

where AR^*_{exp} represents the complex value of the experimentally obtained amplitude ratio. As the value of AR^*_{exp} comes directly from the experiments, it seems adequate to establish the convergence upon the complex amplitude ratio as:

$$\left|\frac{(AR^*_{pp})^{\{i\}}_{calc} - (AR^*_{pp})_{exp}}{(AR^*_{pp})_{exp}}\right| \le tolMin. \tag{10}$$

4.2. Parameters for the numerical calculations

In the present report we have used the geometrical parameters corresponding to the experimental setup of Ref. [18]. Accordingly, we use a cup with radius $R_c = 0.04$ m, and a single-cone bob with a radius $R_b = 0.034$ m and vertical distance to the cup bottom $h = 0.022$ m. The water subphase physical parameters used were $\rho_b = 1000$ kg m^{-3} and $\eta_b = 10^{-3}$ Pa s.

For the dynamical parameters of the rheometer we used the measured values [18] corresponding to the Bohlin C-VOR rheometer at our lab, namely, the moment of inertia of the rotor + bicone assembly, $I = (2.42 \pm 0.02) \times 10^{-5}$ kg m^2, and the coefficient of the frictional torque of the rheometer (C-VOR, Bohlin Instruments), $b = (3.2 \pm 0.5) \times 10^{-8}$ N m s.

Eq. 5 was solved with a mesh having $N = 480$ sub-intervals in the radiate coordinate, $\bar{r}$, and $M = 240$ sub-intervals in the vertical coordinate $\bar{z}$. The value of the tolerance parameter used in Eq.

10 to define convergence of the iterative process was $tolMin = 10^{-5}$, and the maximum number of iterations allowed was 100. According to the results in [20] such values yielded good resolution of the spatial velocity gradients and reasonable convergence times.

4.3. Definition of the direct and inverse numerical problems

The direct problem merely consists in finding the value of the complex amplitude ratio that corresponds to the programmed values of the frequency, ω, and the complex interfacial viscosity, $\eta^*_{s\ prog}$. Hence, it suffices to calculate the corresponding values of the complex Reynolds and Boussinesq numbers, respectively, Re^*_{prog} and Bo^*_{prog}, and to solve Eq. 5 with the boundary conditions specified by Eqs. 6 and 7. Then the numerically obtained complex velocity amplitude function, $g^*_{prog}(\bar{r}, \bar{z})$ is used to calculate the value of the complex amplitude ratio, $AR^*_{prog}(\omega, \eta^*_{s\ prog})$.

Conversely, the inverse problem starts from the numerically obtained values of the complex amplitude ratio, $AR^*_{prog}(\omega, \eta^*_{s\ prog})$, and a suitable seed value of Bo^*, that is obtained using a linear approximation in which the complex velocity amplitude function, $g^*_{clean}(\bar{r}, \bar{z})$, corresponding to a clean interface is used as a first approximation (see Ref. [20] for details). Then Eq. 9 is used to obtain a new calculated value of the Boussinesq number, Bo^*_{calc} and this new value of the Boussinesq number is re-injected into the Boussinesq-Scriven boundary condition, Eq. 7. Solving the hydrodynamic problem again (Eqs. 5, 6, and 7) a new flow field configuration (a new complex velocity amplitude function) is obtained which allows us to compute an iterated value of the complex amplitude ratio through Eq. 8. This procedure is repeated until convergence according to condition Eq. 10 occurs. Then Eq. 9 is used to obtain a converged value of the complex Boussinesq number, Bo^*_{calc}, and a converged value of the complex interfacial viscosity just using the expression $\eta^*_{s\ calc} = R_c \eta^* Bo^*_{calc}$. Throughout this work we have used a convergence tolerance of $tolMin = 10^{-5}$.

The comparison of the complex viscosity values set at the start of the direct problem with the values obtained from the final solution of the inverse problem gives us a way to evaluate the performance of the iterative data processing scheme.

Author Contributions: All authors have contributed equally to this work.

Funding: This research was funded by Ministerio de Economía, Industria y Competitividad, Gobierno de España grant numbers FIS2013-47350-C5-5-R and FIS2017-86007-C3-3-P. P.S.P. was funded by Consejería de Educación, Juventud y Deporte, Comunidad de Madrid, Research Assistant grant number PEJ16/IND/AI-1253.

Acknowledgments: The authors acknowledge the administrative and technical support provided by M.J. Retuerce.

Conflicts of Interest: The authors declare no conflict of interest. The founding sponsors had no role in the design of the study.

Abbreviations

The following abbreviations are used in this manuscript:

ISR	Interfacial Shear Rheometer
DWR	Double wall-ring

References

1. Fuller, G.G.; Vermant, J. Complex Fluid-Fluid Interfaces: Rheology and Structure. *Annual Review of Chemical and Biomolecular Engineering* **2012**, *3*, 519–543. doi:10.1146/annurev-chembioeng-061010-114202.
2. Stetten, A.Z.; Iasella, S.V.; Corcoran, T.E.; Garoff, S.; Przybycien, T.M.; Tilton, R.D. Current Opinion in Colloid & Interface Science Surfactant-induced Marangoni transport of lipids and therapeutics within the lung. *Current Opinion in Colloid & Interface Science* **2018**, *36*, 58–69. doi:10.1016/j.cocis.2018.01.001.
3. Ezuddin, N.S.; Alawa, K.A.; Galor, A. Therapeutic Strategies to Treat Dry Eye in an Aging Population. *Drugs and Aging* **2015**, *32*, 505–513. doi:10.1007/s40266-015-0277-6.

4. Yang, N.; Lv, R.; Jia, J.; Nishinari, K.; Fang, Y. Application of Microrheology in Food Science. *Annual Review of Food Science and Technology* **2017**, *8*, 493–521. doi:10.1146/annurev-food-030216-025859.
5. Sharipova, A.; Aidarova, S.; Mutaliyeva, B.; Babayev, A.; Issakhov, M.; Issayeva, A.; Madybekova, G.; Grigoriev, D.; Miller, R. The Use of Polymer and Surfactants for the Microencapsulation and Emulsion Stabilization. *Colloids and Interfaces* **2017**, *1*, 3. doi:10.3390/colloids1010003.
6. Berton-Carabin, C.C.; Sagis, L.; Schroën, K. Formation, Structure, and Functionality of Interfacial Layers in Food Emulsions. *Annual Review of Food Science and Technology* **2018**, *9*, 551–587. doi:10.1146/annurev-food-030117-012405.
7. Langevin, D.; Argillier, J.f. Interfacial behavior of asphaltenes. *Advances in Colloid and Interface Science* **2016**, *233*, 83–93. doi:10.1016/j.cis.2015.10.005.
8. Erni, P. Deformation modes of complex fluid interfaces. *Soft Matter* **2011**, *7*, 7586–7600. doi:10.1039/c1sm05263b.
9. Liggieri, R.; Miller, L. *Interfacial Rheology*; Brill, 2009. doi:10.1163/ej.9789004175860.i-684.
10. Erni, P.; Fischer, P.; Windhab, E.J.; Kusnezov, V.; Stettin, H.; Läuger, J. Stress- and strain-controlled measurements of interfacial shear viscosity and viscoelasticity at liquid/liquid and gas/liquid interfaces. *Review of Scientific Instruments* **2003**, *74*, 4916–4924. doi:10.1063/1.1614433.
11. Vandebril, S.; Franck, A.; Fuller, G.G.; Moldenaers, P.; Vermant, J. A double wall-ring geometry for interfacial shear rheometry. *Rheologica Acta* **2010**, *49*, 131–144. doi:10.1007/s00397-009-0407-3.
12. Brooks, C.F.; Fuller, G.G.; Frank, C.W.; Robertson, C.R. Interfacial stress rheometer to study rheological transitions in monolayers at the air-water interface. *Langmuir* **1999**, *15*, 2450–2459. doi:10.1021/la980465r.
13. Tajuelo, J.; Pastor, J.M.; Rubio, M.A. A magnetic rod interfacial shear rheometer driven by a mobile magnetic trap. *Journal of Rheology* **2016**, *60*, 1095–1113. doi:10.1122/1.4958668.
14. Edwards, D.A.; Brenner, H.; Wasan, D.T. *Interfacial Transport Processeses and Rheology*; Butterworth-Heinemann: Boston, 1991.
15. Reynaert, S.; Brooks, C.F.; Moldenaers, P.; Vermant, J.; Fuller, G.G. Analysis of the magnetic rod interfacial stress rheometer. *Journal of Rheology* **2008**, *52*, 261–285. doi:10.1122/1.2798238.
16. Verwijlen, T.; Imperiali, L.; Vermant, J. Separating viscoelastic and compressibility contributions in pressure-area isotherm measurements. *Advances in Colloid and Interface Science* **2014**, *206*, 428–436. doi:10.1016/j.cis.2013.09.005.
17. Tajuelo, J.; Pastor, J.M.; Martínez-Pedrero, F.; Vázquez, M.; Ortega, F.; Rubio, R.G.; Rubio, M.A. Magnetic microwire probes for the magnetic rod interfacial stress rheometer. *Langmuir* **2015**, *31*, 1410–1420. doi:10.1021/la5038316.
18. Tajuelo, J.; Rubio, M.A.; Pastor, J.M. Flow field based data processing for the oscillating conical bob interfacial shear rheometer. *Journal of Rheology* **2018**, *62*, 295–311. doi:10.1122/1.5012764.
19. Guzmán, E.; Tajuelo, J.; Pastor, J.M.; Rubio, M.A.; Ortega, F.; Rubio, R.G. Shear rheology of fluid interfaces: Closing the gap between macro- and micro-rheology. *Current Opinion in Colloid & Interface Science* **2018**, *37*, 33–48. doi:10.1016/j.cocis.2018.05.004.
20. Sánchez-Puga, P.; Tajuelo, J.; Pastor, J.M.; Rubio, M.A. BiconeDrag - A data processing application for the oscillating conical bob interfacial shear rheometer, *arXiv:1810.01696*
21. Sanchez-Puga, P.; Tajuelo, J.; Pastor, J.M.; Rubio, M.A. BiconeDrag - A data processing application for the oscillating conical bob interfacial shear rheometer, 2018. doi:10.17632/4TMY9K4YS3.1.